IJASS
International Journal of
Aeronautical and Space Sciences

ORIGINAL PAPER

Effectiveness Analysis of Spin Motion in Reducing Dispersion of Sounding Rocket Flight due to Thrust Misalignment

Vu Dan Thanh Le[1] · Anh Tuan Nguyen[1] · Lac Hong Nguyen[1] · Ngoc Thanh Dang[1] · Ngoc Doan Tran[1] · Jae-Hung Han[2]

Abstract

This paper explores the effectiveness of spin motion in mitigating the flight dispersion of a two-stage solid-propellant rocket model due to thrust misalignment. The aerodynamic coefficients of the rocket model are obtained by the use of a panel method and semi-empirical equations. A simulation program is developed to solve the equations of motion while considering the variations of the inertial parameters. Monte Carlo simulation techniques are applied to provide statistical data that are used to analyze the relationship between the spin motion and flight dispersion. The spin motion is generated by canting the fins to generate the axial aerodynamic moment. The results show that thrust misalignment at the first stage of the rocket has a great impact on the dispersion of rocket flight. By canting the first-stage fins at a relatively large angle to create the spin motion right after launch, the dispersion area of the payload-release location can be minimized considerably. However, thrust misalignment as well as the fin cant angle at the second stage appear to have insignificant effects on the rocket flight trajectory. On the other hand, canting the fins of the second stage at a large angle may lead to an increase in the spin rate, which may be harmful to the rocket operation. The paper also shows the variation of the dispersion characteristics of rocket flight when the fin size is modified.

Keywords Sounding rocket · Thrust misalignment · Rocket flight · Simulation · Flight dispersion

1 Introduction

Sounding rockets are used to carry instruments into the upper atmosphere to reach an altitude of between 40 and 2000 km for research on solar physics, astrophysics, Earth science, geophysics and microgravity [1, 2]. Basically, sounding rockets can be categorized into three types corresponding to the solid, liquid and hybrid motors. For solid-rockets, their engines may produce large thrust, whose misalignment can cause substantial dispersion in the flight data [3]. Thrust misalignment can be understood as the angular offset of the thrust vector from the centerline of the engine. This factor may largely deflect the flight path of a sounding

rocket through pitch and yaw torques that occur about the center of mass. There are many sources of thrust misalignment, such as tolerances on the manufacturing and assembly of rocket motors and nozzles, as well as the distortions of motor cases and changes in nozzle angle as a result of pressurization, etc. [4].

It should be noted that thrust misalignment is only one of many causes of sounding rocket flight dispersion, which are addressed in 14 CFR Part 417 [5] regarding launch safety. The dispersion problem of rocket flight has been investigated and discussed in several previous studies [6–10]. However, in these studies, researchers did not analyze the impact of each factor on the dispersion data separately. Therefore, there have not been any data to indicate to what degree the thrust misalignment factor can account for the overall dispersion of rocket flight. In reality, this kind of data may be a very important basis to set the requirement for the fabrication standard of rocket engines.

To mitigate the effect of thrust misalignment on the flight paths of sounding rockets and other types of spacecraft, spin stabilization techniques are often applied. In recent years,

Vu Dan Thanh Le and Anh Tuan Nguyen are co-first authors.

✉ Anh Tuan Nguyen
  atnguyen@lqdtu.edu.vn

[1] Le Quy Don Technical University, 236 Hoang Quoc Viet, Hanoi, Vietnam

[2] KAIST, Daejeon 34141, Republic of Korea

🙋 Springer

many studies have been conducted to find analytical solutions for the motion of spinning spacecraft with thrust misalignment [11–17]. These research results have indicated that such analytical solutions can provide deeper insight into the behavior of spacecraft motions, and also can be used to develop control algorithms for on-board computers. However, it should be noted that this type of approach does not include the variation of mass and the contribution of aerodynamic loads in the calculation model.

Jarmolow has solved Euler's dynamical equations of the spinning rocket while considering the variation of mass and the torque produced by thrust misalignment [18]. The solution was compared with that in a case of constant mass and torque. The characteristics of the two types of solutions were found very different, which deduces that in rocket motion analyses, the variations of mass and torque produced by thrust misalignment cannot be neglected.

Papis et al. have done research on attitude dispersion of a spinning rocket in vacuum under various angular disturbances [19]. The solutions from the equations of motion were derived by employing a numerical integration and a Monte Carlo technique. However, it is noteworthy that compared to actual rocket flight, the problem in their study is considerably simplified since no aerodynamic force is included.

Due to the nonlinear effects of input perturbations on sounding rocket trajectories, a full six-degrees-of-freedom (6-DOF) dynamic model is usually required together with Monte Carlo simulation techniques to obtain the accurate statistical properties of flight path dispersion [20]. However, in all previous studies on spinning-rocket flight with thrust misalignment, researchers have not provided complete 6-DOF models that involve the effects of aerodynamic loads and the variations of the rocket's inertial parameters.

In this paper, the 6-DOF model of a two-stage solid-propellant sounding rocket is built in multibody dynamics simulation software MSC Adams. Aerodynamic forces and moments are calculated using a constant-pressure panel method proposed by Woodward [21] in combination with the semi-empirical method of Lebedev [22]. The effects of the variations of the inertial properties and the center of mass are taken into consideration in this study. Firstly, an analysis is carried out to find out how the fin cant angles affect the spin motion of the rocket model. Next, Monte Carlo simulation techniques are applied to assess to what degree the flight dispersion of the rocket due to thrust misalignment can be reduced by the spin motion through canting the fins. In the present paper, a complete integrated computational model, which includes the details of the aerodynamic loads, the variations of the inertial parameters, and the full 6-DOF equations of motion, is developed for a multi-stage sounding rocket model while statistically studying the effect of thrust misalignment. The model is built in the environment of MSC Adams software, and a series of user-defined functions and subroutines are added to the software to make it applicable to multi-stage rocket flight simulation. This is the first time MSC Adams software has been customized to be used for this kind of simulation task. In this work, a wide range of data related to the spin rate of the rocket and dispersion areas are obtained and intensively analyzed in an effort to find appropriate cant angles to enhance the quality of sounding rocket flight while thrust misalignment occurs at all stages. In addition, the fin size effect on the dispersion characteristics of rocket flight is numerically studied and discussed in this paper.

2 Rocket Modeling and Simulation Methodology

2.1 Rocket Modeling

The solid-propellant sounding rocket model studied in this work is composed of two stages as shown in Fig. 1. The subscript G refers to the ground-fixed coordinate system. In this study, the origin of the coordinate system is located at the launch point; the positive z_G axis points vertically downward, and the rocket is launched toward the x_G axis. Some main parameters of the rocket are presented in Table 1.
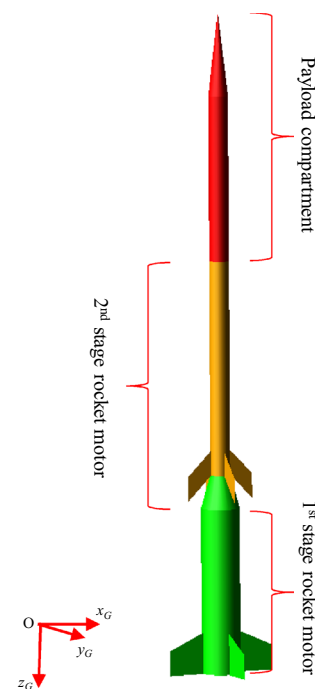

Fig. 1 The sounding rocket model

Table 1 Main parameters of the rocket model

Initial mass (kg)	92.0
Mass of the 1st stage (kg)	55.0
Mass of the 1st stage without propellant (kg)	26.0
Mass of the 2nd stage (kg)	37.0
Mass of the 2nd stage without propellant (kg)	14.7
Total length (m)	4.0
1st stage diameter (m)	0.235
2nd stage diameter (m)	0.12
Length of the nose cone (m)	0.5
1st stage wing's leading-edge location (from the nose tip) (m)	3.75
1st stage wing's length (m)	0.22
1st wing's root chord (m)	0.25
1st wing's tip chord (m)	0.15
1st wing's sweep angle (deg.)	24.4
2nd stage wing's leading-edge location (m)	2.65
2nd stage wing's length (m)	0.15
2nd wing's root chord (m)	0.15
2nd wing's tip chord (m)	0.15
2nd wing's sweep angle (deg.)	45
1st stage thrust (N)	19,300
2nd stage thrust (N)	5,950
1st stage burn time (s)	2.8
2nd stage burn time (s)	4.6
Specific impulse (s)	190

The sounding rocket is launched at an angle of 85°, and the first stage separates immediately after it runs out of fuel. The ignition of the second-stage motor is delayed by 18 s after the separation of the first stage. The purpose of this delay is to enhance the maximum altitude of the rocket. In this work, we study the flight path of the rocket within the first 100 s. It is assumed that after this period of time, the 12-kg payload compartment separates from the second-stage motor and is then recovered by a parachute system. For simplicity, the effect of separation impulses is neglected in this study.

2.2 Aerodynamic Model

The aerodynamic coefficients of the present sounding rocket model are computed through the combination of Woodward's panel method [21] and semi-empirical equations [22, 23]. The code of Woodward's panel method is written in FORTRAN and available in [24]. In this work, the original panel code is improved by increasing the maximum allowed number of panels and enabling the program to work on asymmetric aerodynamic problems. The present rocket model operates at low angles of attack, so the linear superposition principle can be applied to the prediction processes of the aerodynamic coefficients as

$$
\begin{aligned}
C_x &= C_{x0}^f + C_{x0}^p + C_{x0}^b + C_{xi_\alpha}\alpha^2 + C_{xi_\delta}\delta^2, \\
C_z &= C_{z_\alpha}\alpha + C_{z_{\omega_y^*}}\omega_y^*, \\
m_x &= m_{x_{\omega_x^*}}\omega_x^* + m_{x_\delta}\delta \\
m_y &= m_{y_\alpha}\alpha + m_{y_{\omega_y^*}}\omega_y^*,
\end{aligned}
\tag{1}
$$

where C_x and C_z denote the force coefficients along the x_b and z_b axes of the body-fixed coordinate system. m_x and m_y are the moment coefficients about the x_b and y_b axes. α, ω and δ respectively represent the angle of attack, the angular velocity of the rocket and the cant angle of the fins used to control the spin motion. The superscripts f, p and b refer to the skin-friction drag, pressure drag and base drag, respectively. C_{xi_α} and C_{xi_δ} are the coefficients related to the induced drag components when the angle of attack and the fin cant angles are nonzero. Here, the area and the radius of the second stage's cross-section are respectively used as the reference area and the reference length when defining the aerodynamic coefficients. In Eq. (1), the superscript * represents the nondimensional quantity, which is expressed as

$$
\omega^* = \omega\frac{l_{\mathrm{ref}}}{2V_\infty},
\tag{2}
$$

where l_{ref} is the reference length, which is equal to the radius of the second stage's cross-section; and V_∞ is the freestream velocity.

The body-fixed coordinate system is illustrated in Fig. 2. The x_b axis is placed along the body axis of the rocket and points toward the nose tip. Before launch, the rocket has an initial pitch angle as shown in the figure.

First of all, the equivalent cruciform models, which consist of constant-pressure panels, are created as shown in Fig. 3 to compute all of the aerodynamic coefficients mentioned in Eq. (1) except for the skin-friction drag, pressure drag and base drag coefficients. The pressure difference on each panel is computed using the non-penetration boundary condition. Expressions related to the velocity field induced by a constant-pressure panel are provided in the literature [21]. It is noteworthy that for a conventional rocket model with a revolved body, Woodward's panel method tends to underestimate the lift force. Woodward used line sources to model revolved bodies and treated them as non-lifting objects. Therefore, lift generated by the body in this type of model appears to be lower than the actual value. Using the cruciform models as shown in Fig. 3, this problem can be solved, and the lift force prediction becomes more accurate.
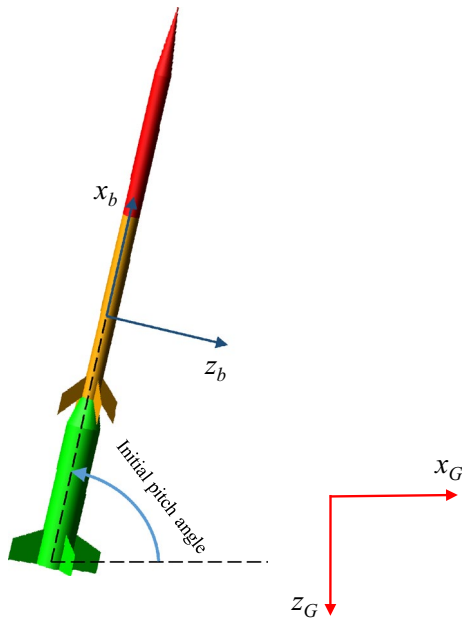
Fig. 2 The body-fixed coordinate system of the rocket before launch

The pressure distribution on the rocket body surface is then computed by the line-source-based aerodynamic model [21]. By integrating this distribution we can obtain the pressure drag coefficient C_{x0}^p. The base drag coefficient C_{x0}^b, which occurs when the rocket engine is off, is determined by the following semi-empirical equation:

$$C_{x0}^b = k_{\text{base}} \frac{S_{\text{base}}}{S_0}, \tag{3}$$

where k_{base} is a coefficient that depends on the Mach number and the geometry of the base. The value of this coefficient is determined by a look-up table given in the literature [22].

Fleeman's equation is used to determine the skin-friction drag coefficient C_{x0}^f as follows [23]:

$$C_{x0}^f = 0.053 \frac{l}{d} \left(14.6 \frac{M}{ql} \right)^{0.2}, \tag{4}$$
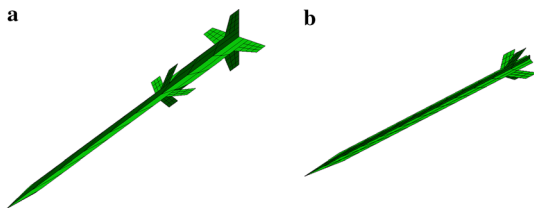
Fig. 3 The cruciform models of the all-stage rocket model (**a**) and its second stage (**b**)

where l and d are the length and the diameter of the rocket, respectively; M is the Mach number; and q denotes the dynamic pressure.

To validate the aerodynamic model used in this study, we compare aerodynamic coefficients of the "stage 2 and 3" model of a theater ballistic missile target with those from a wind tunnel experiment [25]. A good agreement, which is observed in Fig. 4, confirms the validity of the present aerodynamic model.

Applying the present method to the sounding rocket shown in Fig. 1, the aerodynamic coefficients in Eq. (1) can be determined and some of them are plotted against the Mach number in Fig. 5. Here, C_{x0} denotes the total drag at a zero angle of attack and zero fin cant angles, and δ_1 and δ_2 are the cant angles at the first and second stages, respectively. In this figure, the moment coefficients before and after the stage separation event are calculated with respect to the centers of mass of the full rocket model and the second stage before burn, respectively. According to these data, for the full rocket model before the burning of the first-stage propellant, the location of the center of pressure is about 0.42 m behind the center of mass; and this distance slightly increases to 0.44 m when the propellant completely burns out at a Mach number of about 1.8. For the second stage, right after the stage separation event, the center of pressure is located 0.58 m behind the center of mass. When the second-stage motor stops working, the rocket reaches the highest speed at a Mach number of about 3.0, and the distance
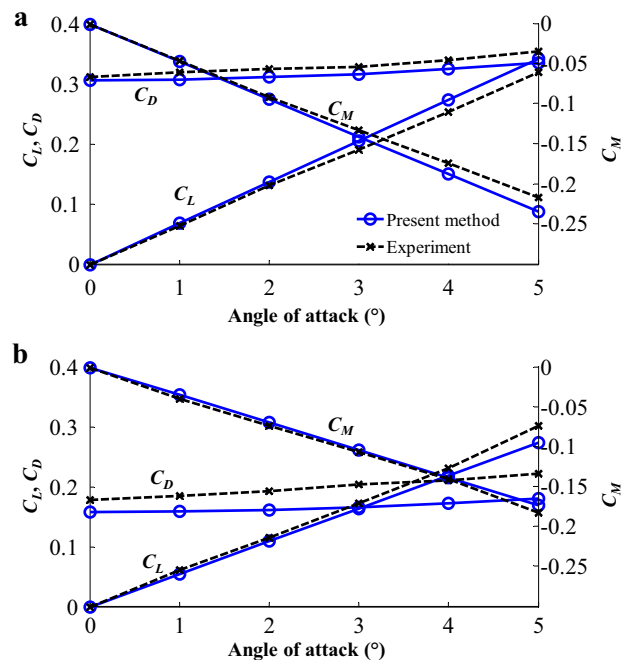
Fig. 4 Aerodynamic coefficients from the present method and from an experiment at Mach numbers of 2.5 (**a**) and 4.0 (**b**)
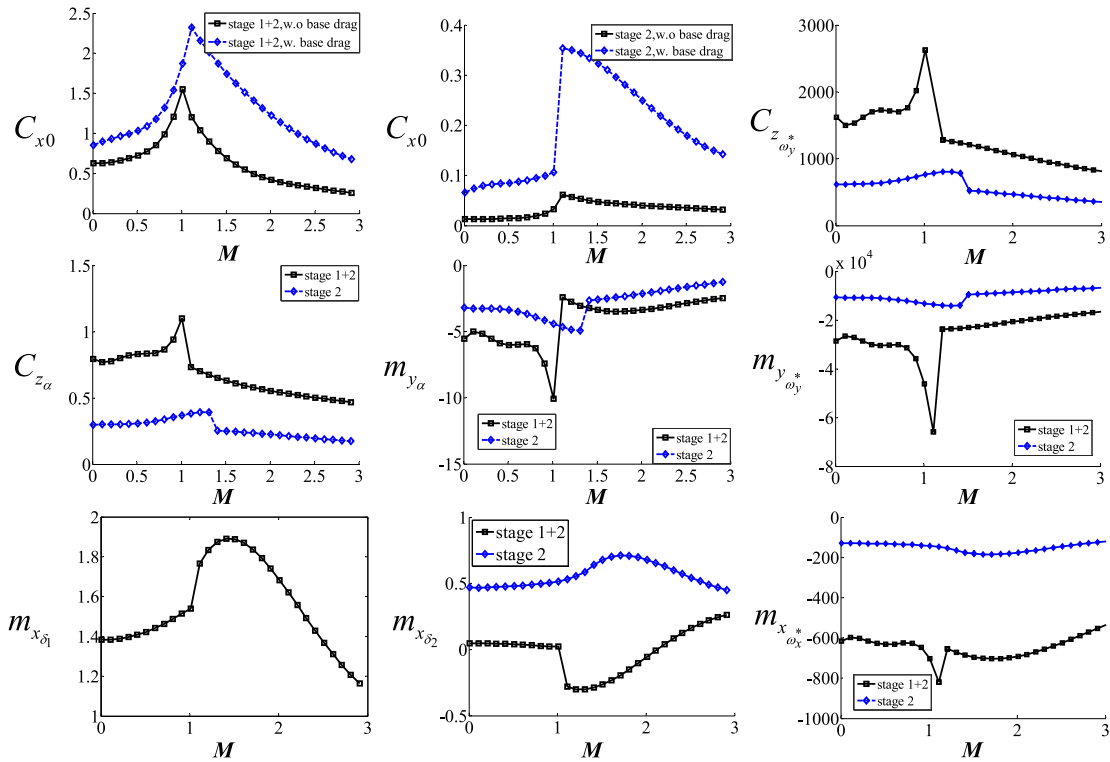
Fig. 5 Aerodynamic coefficients of the sounding rocket model against the Mach number
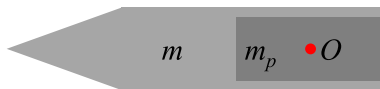

Fig. 6 Illustration of a rocket and its propellant grain

between the center of pressure and center of mass enlarges to 0.74 m. Based on these data, it obvious that the rocket is statically stable.

2.3 Rocket Dynamics Model

2.3.1 The Development of the Dynamics Model

Compared to previous rocket dynamics simulation studies [26–31], the present dynamics model can include the effects of the variations of the rocket's inertial properties based on the use of Thomson's equations for a variable-mass system [32]. Figure 6 shows an illustration of a rocket with total mass of m, and the mass of its propellant grain is m_p. It is assumed that the grain burns in a manner that the location of its center of mass does not change. Therefore, according to Eke [33], the current rocket motor may burn in one of the following scenarios: the uniform burn, the radial burn and the centripetal burn. Let the center of mass of the grain O

be the reference point to study the dynamics of the rocket model. According to Thomson [32], the force equation is

$$\boldsymbol{F}^b = m\ddot{\boldsymbol{r}}_c^b - \ddot{m}\left(\boldsymbol{r}_{Oe}^b - \boldsymbol{r}_{Oc}^b\right) - \dot{m}\left(2\boldsymbol{\omega}^b \times \left(\boldsymbol{r}_{Oe}^b - \boldsymbol{r}_{Oc}^b\right) - 2\frac{d\boldsymbol{r}_{Oc}^b}{dt} + \boldsymbol{u}^b\right),$$

(5)

where superscript b refers to the body-fixed coordinate system, $\boldsymbol{F}$ denotes the external force, m is the mass of the rocket, $\boldsymbol{r}$ is the position vector, $\boldsymbol{u}$ is the velocity of ejected mass relative to the rocket, $\boldsymbol{\omega}$ is the angular velocity of the rocket, and O, c and e respectively represent the reference point, the center of mass of the rocket and the location where mass is ejected.

The velocity of the center of mass $\boldsymbol{r}_c^b$ can be expressed as

$$\dot{\boldsymbol{r}}_c^b = \dot{\boldsymbol{r}}_O^b + \boldsymbol{\omega}^b \times \boldsymbol{r}_{Oc}^b + \frac{d\boldsymbol{r}_{Oc}^b}{dt}.$$

(6)

Then

$$\ddot{\boldsymbol{r}}_c^b = \ddot{\boldsymbol{r}}_O^b + \dot{\boldsymbol{\omega}}^b \times \boldsymbol{r}_{Oc}^b + 2\boldsymbol{\omega}^b \times \frac{d\boldsymbol{r}_{Oc}^b}{dt} + \boldsymbol{\omega}^b \times \left(\boldsymbol{\omega}^b \times \boldsymbol{r}_{Oc}^b\right) + \frac{d^2\boldsymbol{r}_{Oc}^b}{dt^2}.$$

(7)

During the burning process of the motor, the center of mass of the grain always coincides with O, then $\boldsymbol{r}_{Oc}^b$ can be defined as

$$\boldsymbol{r}_{Oc}^b = \frac{m_0 \boldsymbol{r}_{Oc_0}^b}{m}, \tag{8}$$

where m_0 and c_0 denote the mass and the center of mass of the system before the burn.

Substituting Eq. (8) into Eq. (7), we derive

$$\ddot{\boldsymbol{r}}_c^b = \ddot{\boldsymbol{r}}_O^b + \frac{m_0}{m}\dot{\boldsymbol{\omega}}^b \times \boldsymbol{r}_{Oc_0}^b + 2\boldsymbol{\omega}^b \times \frac{d\boldsymbol{r}_{Oc}^b}{dt} \\ + \frac{m_0}{m}\boldsymbol{\omega}^b \times \left(\boldsymbol{\omega}^b \times \boldsymbol{r}_{Oc_0}^b \right) + \frac{d^2\boldsymbol{r}_{Oc}^b}{dt^2}. \tag{9}$$

Then

$$m\ddot{\boldsymbol{r}}_c^b = m\ddot{\boldsymbol{r}}_O^b + m_0\dot{\boldsymbol{\omega}}^b \times \boldsymbol{r}_{Oc_0}^b + 2m\boldsymbol{\omega}^b \\ \times \frac{d\boldsymbol{r}_{Oc}^b}{dt} + m_0\boldsymbol{\omega}^b \times \left(\boldsymbol{\omega}^b \times \boldsymbol{r}_{Oc_0}^b \right) + m\frac{d^2\boldsymbol{r}_{Oc}^b}{dt^2}. \tag{10}$$

Replacing $m\ddot{\boldsymbol{r}}_O^b$ by $(m_0 - \Delta m)\ddot{\boldsymbol{r}}_O^b$, where Δm is the mass loss during the burn, we then derive

$$m\ddot{\boldsymbol{r}}_c^b = m_0\left[\ddot{\boldsymbol{r}}_O^b + \dot{\boldsymbol{\omega}}^b \times \boldsymbol{r}_{Oc_0}^b + \boldsymbol{\omega}^b \times \left(\boldsymbol{\omega}^b \times \boldsymbol{r}_{Oc_0}^b \right) \right] \\ + 2m\boldsymbol{\omega}^b \times \frac{d\boldsymbol{r}_{Oc}^b}{dt} + m\frac{d^2\boldsymbol{r}_{Oc}^b}{dt^2} - \Delta m\ddot{\boldsymbol{r}}_O^b. \tag{11}$$

It is easy to find that $\ddot{\boldsymbol{r}}_O^b + \dot{\boldsymbol{\omega}}^b \times \boldsymbol{r}_{Oc_0}^b + \boldsymbol{\omega}^b \times \left(\boldsymbol{\omega}^b \times \boldsymbol{r}_{Oc_0}^b \right)$ is an expression of $\ddot{\boldsymbol{r}}_{c_0}^b$. Therefore,

$$m\ddot{\boldsymbol{r}}_c^b = m_0\ddot{\boldsymbol{r}}_{c_0}^b + 2m\boldsymbol{\omega}^b \times \frac{d\boldsymbol{r}_{Oc_0}^b}{dt} + m\frac{d^2\boldsymbol{r}_{Oc_0}^b}{dt^2} - \Delta m\ddot{\boldsymbol{r}}_O^b. \tag{12}$$

Substituting Eq. (12) into Eq. (5), we can obtain

$$\boldsymbol{F}^b = m_0\ddot{\boldsymbol{r}}_{c_0}^b + 2m\boldsymbol{\omega}^b \times \frac{d\boldsymbol{r}_{Oc}^b}{dt} + m\frac{d^2\boldsymbol{r}_{Oc}^b}{dt^2} - \Delta m\ddot{\boldsymbol{r}}_O^b - \ddot{m}\left(\boldsymbol{r}_{Oe}^b - \boldsymbol{r}_{Oc}^b \right) \\ - \dot{m}\left(2\boldsymbol{\omega}^b \times \left(\boldsymbol{r}_{Oe}^b - \boldsymbol{r}_{Oc}^b \right) - 2\frac{d\boldsymbol{r}_{Oc}^b}{dt} + \boldsymbol{u}^b \right). \tag{13}$$

It is assumed that the thrust force $\boldsymbol{F}_T$ is independent of the flight condition and always equal to $\dot{m}\boldsymbol{u}$. Here, it is noted that $\dot{m}$ is negative during the burning process; thus, $\boldsymbol{F}_T$ has an opposite direction to the relative ejection velocity $\boldsymbol{u}$. Thus,

$$\boldsymbol{F}^b + \boldsymbol{F}_T^b + \Delta m\ddot{\boldsymbol{r}}_O^b - 2m\boldsymbol{\omega}^b \times \frac{d\boldsymbol{r}_{Oc}^b}{dt} - m\frac{d^2\boldsymbol{r}_{Oc}^b}{dt^2} + \ddot{m}\left(\boldsymbol{r}_{Oe}^b - \boldsymbol{r}_{Oc}^b \right) \\ + \dot{m}\left(2\boldsymbol{\omega}^b \times \left(\boldsymbol{r}_{Oe}^b - \boldsymbol{r}_{Oc}^b \right) - 2\frac{d\boldsymbol{r}_{Oc}^b}{dt} \right) = m_0\ddot{\boldsymbol{r}}_{c_0}^b. \tag{14}$$

From Eq. (8), it follows that $m\boldsymbol{r}_{Oc}^b = m_0\boldsymbol{r}_{Oc_0}^b$, which is a constant. Therefore, the first and second derivatives of $m\boldsymbol{r}_{Oc}^b$ are zero, which means

$$\dot{m}\boldsymbol{r}_{Oc}^b + m\frac{d\boldsymbol{r}_{Oc}^b}{dt} = 0, \\ \ddot{m}\boldsymbol{r}_{Oc}^b + 2\dot{m}\frac{d\boldsymbol{r}_{Oc}^b}{dt} + m\frac{d^2\boldsymbol{r}_{Oc}^b}{dt^2} = 0. \tag{15}$$

Substituting Eq. (15) into Eq. (14), the force equation could be simplified as follows:

$$\boldsymbol{F}^b + \boldsymbol{F}_T^b + \Delta m\ddot{\boldsymbol{r}}_O^b + \ddot{m}\boldsymbol{r}_{Oe}^b + 2\dot{m}\boldsymbol{\omega}^b \times \boldsymbol{r}_{Oe}^b = m_0\ddot{\boldsymbol{r}}_{c_0}^b. \tag{16}$$

In Eq. (16), the first two terms in the left-hand side are the external and thrust forces while the remaining three terms are from the mass variation effect. Without these three terms, Eq. (16) becomes the force equation of a constant-mass system. Compared to Eq. (5), all of the terms in Eq. (16) are expressed about points O or c_0, which are fixed to the rocket body.

Similarly, the moment equation is derived on the basis of Thomson's work [32]. The original equation is

$$\boldsymbol{M}_O^b = -m\ddot{\boldsymbol{r}}_O^b \times \boldsymbol{r}_{Oc}^b + \mathbf{I}^b\frac{d\boldsymbol{\omega}^b}{dt} + \boldsymbol{\omega}^b \times \left(\mathbf{I}^b\boldsymbol{\omega}^b \right) \\ + 2\sum_B m_i\boldsymbol{r}_{Oi}^b \times \left(\boldsymbol{\omega}^b \times \frac{d\boldsymbol{r}_{Oi}^b}{dt} \right) \\ + \sum_B m_i\boldsymbol{r}_{Oi}^b \times \frac{d^2\boldsymbol{r}_{Oi}^b}{dt^2} - \sum_S \dot{m}_i\boldsymbol{r}_{Oi}^b \times \boldsymbol{u}_i^b, \tag{17}$$

where B is a closed boundary surface within which we define the variable-mass system, and S is the surface where particles cross over B. $\mathbf{I}^b$ denotes the moment of inertia of the rocket about point O in the body-fixed coordinate system. For simplicity, we assume that inside the motor, all particles are distributed symmetrically and move uniformly at a constant speed. Therefore, the terms $2\sum_B m_i\boldsymbol{r}_{Oi}^b \times \left(\boldsymbol{\omega} \times \frac{d\boldsymbol{r}_{Oi}^b}{dt} \right)$ and $\sum_B m_i\boldsymbol{r}_{Oi}^b \times \frac{d^2\boldsymbol{r}_{Oi}^b}{dt^2}$ are equal to zero. The term $\sum_S \dot{m}_i\boldsymbol{r}_{Oi}^b \times \boldsymbol{u}_i^b$ is the moment $\boldsymbol{M}_T^b$ generated by the thrust force about point O expressed in the body-fixed coordinate system. Hence, Eq. (17) can be reformed as

$$\boldsymbol{M}_O^b = -m\ddot{\boldsymbol{r}}_O^b \times \boldsymbol{r}_{Oc}^b + \mathbf{I}^b\frac{d\boldsymbol{\omega}^b}{dt} + \boldsymbol{\omega}^b \times \left(\mathbf{I}^b\boldsymbol{\omega}^b \right) - \boldsymbol{M}_T. \tag{18}$$

Replacing m by $m_0 - \Delta m$ and $\mathbf{I}^b$ by $\mathbf{I}_0^b - \Delta\mathbf{I}^b$, and taking Eq. (8) into account, we can obtain the following moment equation:

$$M_O^b + M_T^b + \Delta \mathbf{I}^b \frac{d\boldsymbol{\omega}^b}{dt} + \boldsymbol{\omega}^b \times \left(\Delta \mathbf{I}^b \boldsymbol{\omega}^b \right)$$

$$= -m_0 \ddot{\boldsymbol{r}}_O^b \times \boldsymbol{r}_{Oc_0}^b + \mathbf{I}_0^b \frac{d\boldsymbol{\omega}^b}{dt} + \boldsymbol{\omega}^b \times \left(\mathbf{I}_0^b \boldsymbol{\omega}^b \right). \tag{19}$$

Here, $\mathbf{I}_0^b$ and $\Delta \mathbf{I}^b$ are the initial moment of inertia and its loss due to the burn, respectively.

The last two terms in the left-hand side of Eq. (19) are related to the variations of the rocket's inertial properties. Similar to the force equation [Eq. (16)], using Eq. (19), the moment equation is expressed in a preferable form about points O and c_0, which are fixed to the rocket body. Compared to their original forms [Eqs. (5) and (17)], the new force and moment equations [Eqs. (16) and (19)] can be handled more easily. In these equations, the six-degrees-of-freedom comprise three translational displacements and three Euler angles to determine the position and the attitude of the rocket, respectively. The expression of a vector in the body-fixed coordinate system can be converted to that in the ground-fixed coordinate system through a direction cosine matrix and vice versa. In this study, the solutions from Eqs. (16) and (19) are obtained in the MSC Adams environment using the GSTIFF integrator with the prediction and correction phases [34]. MSC Adams solver was not created to deal with variable-mass problems. To overcome this challenge, a novel idea is applied to customize the program by putting all of the terms related to the variations of the mass and the moment of inertia in Eqs. (16) and (19) to the solver in the forms of external forces and moments. Additionally, the solver also includes the contributions of the aerodynamic loads and thrust. The aerodynamic force and moment are calculated based on the model presented in Sect. 2.2. It should be noted that the change in the gravitational force due to mass loss is also considered separately in the simulation program.

2.3.2 Validation of the Dynamics Model

To validate the present dynamics model, we study a case of a simple rocket that has an initial mass of 70 kg. The rocket propellant grain weighs 20 kg and the burn time is 2.0 s. The grain is assumed small and its center of mass is located near the motor nozzle as shown in Fig. 7. The thrust is assumed constant and equal 20,000 N. The rocket is launched vertically, and a small lateral force of 10 N is applied to the model to curve the trajectory. Here, for the sake of simplicity, the aerodynamic loads are not considered.

Fig. 7 A simple rocket model with grain

Firstly, the solution for the dynamics problem is obtained by the simulation program described in Sect. 2.3.1. Then, this solution is compared with that of an MSC Adams program using an emulated rocket motor. For the rocket emulation program, the grain is discretized into particles that leave the nozzle one after another. Right after a particle leaves the nozzle, its connection to the rocket is deactivated, and the total mass of the system is reduced. Applying this technique, these particles are used to emulate the product of combustion that happens in the rocket motor (Fig. 8). In the present study, 10 particles are employed for the emulation purpose.

The solution from Eqs. (16) and (19) for the first two seconds shows a very good agreement with that by the emulation program (Fig. 9). The most noticeable differences are found in the translational and angular acceleration plots, which are explained by the discretization technique used in the emulation program. However, the overall trends of the two types of solutions are very close, which can confirm the validity of the present rocket dynamics model.

3 Results and Discussion

3.1 The Effect of Canted Fins on the Spin Rate

As mentioned earlier, to cancel out the unfavorable effects of asymmetric conditions, such as thrust misalignment on the flight trajectory of the rocket, the fins are deliberately canted to generate the spin motion of the rocket. In this subsection, we investigate the relationship between the fin cant angles and the rocket spin rate. It is assumed that the fins at the first and second stages of the rocket may be canted up to 0.5°.

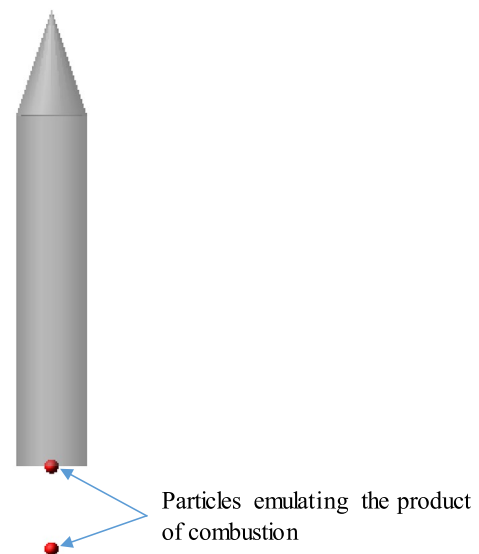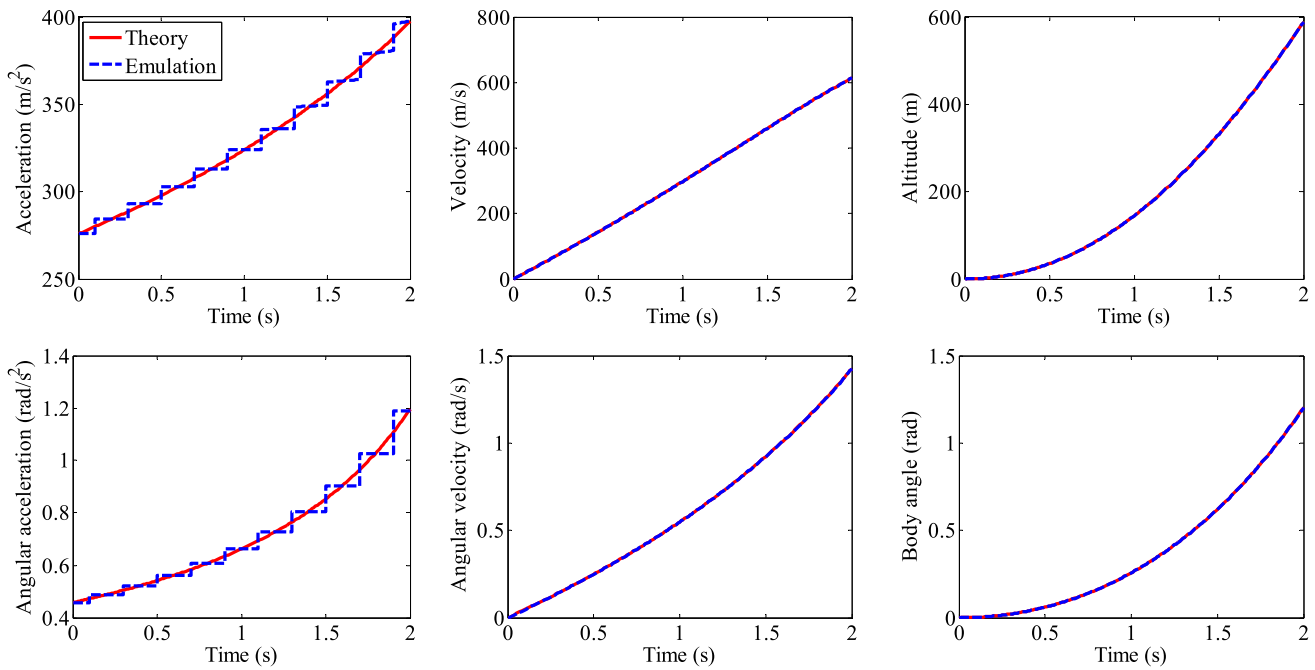Particles emulating the product of combustion

**Fig. 8** Rocket and particles in the rocket emulation program

Fig. 9 Solution from Eqs. (16) and (19) (theory) and that by the emulation program

Figure 10 shows the 40-s time histories of the rocket speed and the variations of the spin rate for several combinations of the first- and second-stage cant angles δ_1 and δ_2. Based on our observations, after 40 s the spin rate monotonously decreases for all cases. It is noted that thrust misalignment is not included here, and the cant angles do not have any significant effect on the rocket speed. In general, the spin rate follows the trend of the speed. It is found that the spin rate grows rapidly when the rocket is accelerated during the motor burn. The separation of the first stage is followed by a rapid increase in the spin rate. This increase could be explained by a sudden reduction in the spin-damping coefficient $m_{x_{\omega_x^*}}$ after the separation, which is exhibited in Fig. 5.

As shown in Fig. 5, $m_{x_{\delta_2}}$ may have a negative value when the Mach number above 1.0 for the all-stage configuration, which signifies a roll reversal effect [35]. This effect can be observed before the separation of the first stage in Fig. 10 when $\delta_1 = 0$. A negative value of the spin rate is induced by the deflections of the second stage's fins according to the roll reversal effect.

Tables 2 and 3 present the maximum spin rates with respect to various combinations of δ_1 and δ_2 during the burns of the first- and second-stage motors, respectively. It is seen that for most cases, the maximum spin rate during the burn of the second-stage motor is larger, which is attributed to the higher speed of the rocket and the lower absolute value of the spin-damping coefficient $m_{x_{\omega_x^*}}$ at this phase. The spin rate of the rocket can be calculated by the following equation:
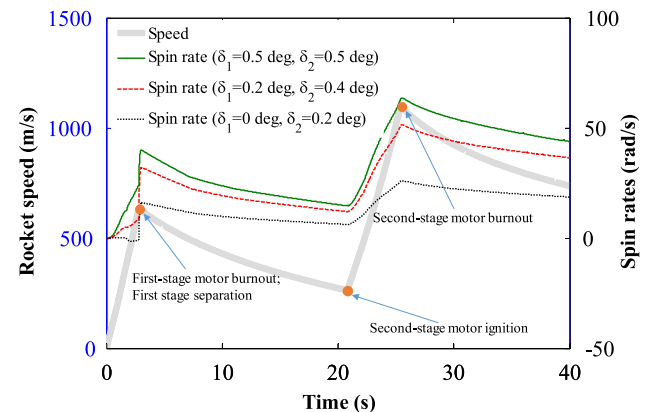
Fig. 10 Rocket speed and spin rates against time

$$-m_{x_{\omega_x^*}} \omega_x \frac{l_{\text{ref}}}{2V} = m_{x_\delta} \delta. \tag{20}$$

The left-hand side of the above equation is the aerodynamic spin-damping moment while the right-hand side expresses the aerodynamic moment arising from the cant angles of the fins. From Eq. (20), it follows that

$$\omega_x = \frac{-2V m_{x_\delta} \delta}{m_{x_{\omega_x^*}} l_{\text{ref}}}. \tag{21}$$

It is obvious that at a higher speed V and a lower absolute value of the spin-damping coefficient $m_{x_{\omega_x^*}}$, the spin rate ω_x is larger. Figure 11 shows the maximum spin rates

**Table 2** Maximum spin rates before the separation of the first-stage motor

$\delta_1(°)/\delta_2(°)$	0	0.1	0.2	0.3	0.4	0.5
0	0.00	5.25	10.51	15.77	21.02	26.27
0.1	0.67	4.83	10.09	15.35	20.6	25.86
0.2	1.33	4.41	9.67	14.93	20.18	25.44
0.3	2.00	3.99	9.25	14.51	19.76	25.02
0.4	2.66	3.75	8.83	14.09	19.34	24.60
0.5	3.33	4.08	8.41	13.67	18.92	24.17

Table 3 Maximum spin rates after the separation of the first-stage motor

$\delta_1(°)/\delta_2(°)$	0	0.1	0.2	0.3	0.4	0.5
0	0.00	0.00	0.00	0.00	0.00	0.00
0.1	12.94	12.94	12.94	12.94	12.94	12.94
0.2	25.88	25.87	25.87	25.88	25.88	25.88
0.3	38.83	38.81	38.82	38.83	38.83	38.83
0.4	51.77	51.75	51.74	51.75	51.75	51.76
0.5	64.69	64.7	64.67	64.67	64.68	64.68

based on the data given in Tables 2 and 3. It is observed that while the maximum spin rate during the burn of the second-stage motor ω_2 almost depends only on the cant angle of the second-stage fins δ_2, the maximum spin rate during the burn of the first-stage motor ω_1 can be determined mainly based on the value of the first-stage fin angle δ_1. However, δ_2 also has a slight influence on the value of ω_1. This influence comes from the roll reversal effect as mentioned earlier, which means with an increase of δ_2, the maximum spin rate during the burn of the first-stage motor ω_1 decreases. It should be noted that a too large value of the maximum spin rate should be prevented to avoid any excessive centrifugal acceleration that may cause severe damages to the rocket structures and the on-board equipment.
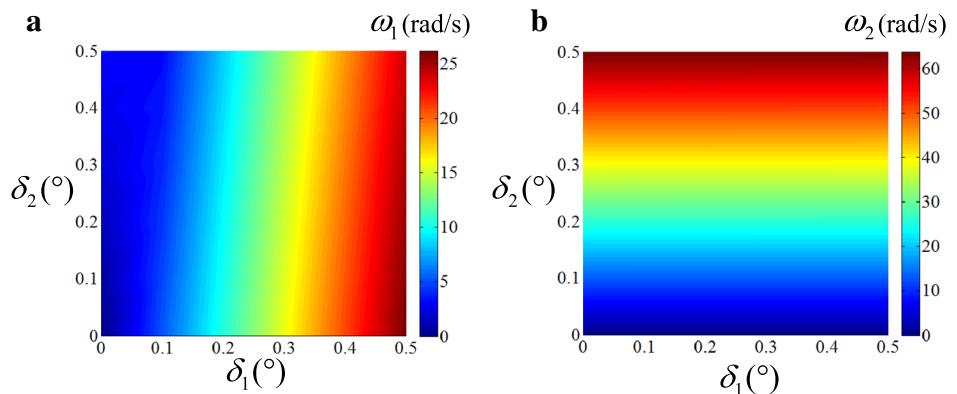
3.2 Thrust Misalignment Generation and Flight Dispersion Reduction

3.2.1 Random Thrust Misalignment Generation

As mentioned earlier in this paper, there are many sources of thrust misalignment, which may cause unpredictable negative effects on sounding rocket trajectories. Figure 12 shows angles φ and θ that are used to define the thrust misalignment. For vertical launch, when θ equals 0, the thrust vector lies on the $x_G O z_G$ plane (Fig. 1). It is assumed that for the first- and second-stage rocket motors, φ has the same Gaussian distribution with the mean value of 0 and a standard deviation of 0.1°. These values are selected based on a study of Knauber [4], who stated that most fixed-nozzle solid rocket motors have a thrust misalignment of less than 0.25°. The angle θ takes a uniform distribution within 0 to 180°. In this work, 100 sets of the misalignment angles, which encompass the angles φ and θ of the first- and second-stage rocket motors, are generated randomly and presented in Fig. 13. Figure 14 shows the thrust misalignment histograms at the first and second stages, which are represented by the absolute value of φ. The histograms of the generated data are close to the theoretical ones, which are built based on the Gaussian distribution of φ.

3.2.2 Flight Dispersion of the Non-Spinning Rocket

100 random data sets of thrust misalignment shown in Fig. 13 are applied to the present sounding rocket model to study the dispersion of its flight. In this study, the effect of thrust misalignment on rocket flight is investigated through the dispersion of the payload-release point. The rocket is assumed to be launched from the origin of the ground-fixed coordinate system $x_G y_G z_G$ at an angle of 85° towards the x_G direction, and the payload is released 100 s after launch. The dispersion is characterized by the area an ellipse that is expected to cover 95% of the probable cases. This ellipse
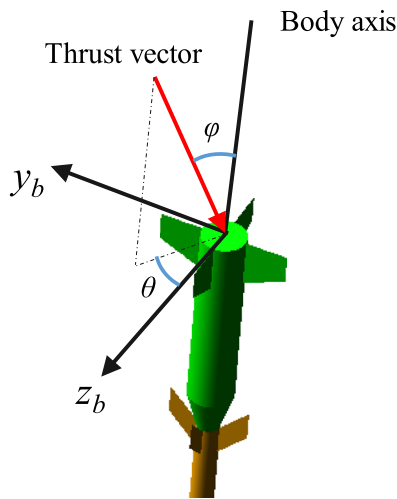

Fig. 11 Maximum spin rates before (**a**) and after (**b**) the separation of the first-stage motor at various values of δ_1 and δ_2

Fig. 12 Angles used to define the thrust misalignment

Fig. 14 The thrust misalignment histograms of the first- (**a**) and second-stage (**b**) motors
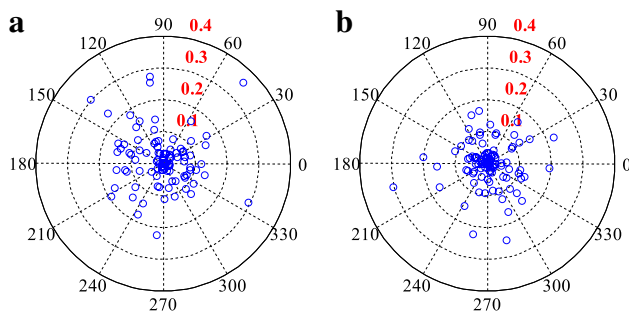

Fig. 13 Thrust misalignment angles of the first- (**a**) and second-stage (**b**) motors

is called a 95% confidence ellipse, whose properties can be found in the literature [36].

Figure 15 presents the dispersion data for several cases of thrust misalignment with their 95% confidence ellipses. The expected release point of the payload is 12.2 km from the launch point along the x_G axis. The ellipse area corresponding to thrust misalignment occurring at both stages is 167.8 km^2, which is slightly larger than an area of 165.3 km^2 in the case of the first-stage thrust misalignment. At the same time, the area of the 95% confidence ellipse corresponding to the second-stage thrust misalignment is only 1.2 km^2. Hence, it is relevant to state that thrust misalignment at the second stage has a minimal effect on the dispersion of rocket flight. The main source of the total dispersion is the first-stage thrust misalignment, which accounts for 98.5% of the area of the 95% confidence ellipse.

According to Boersma et al. [7] and 14 CFR Part 420 [37], the impact dispersion radius of unguided rockets is from 20 to 40% of the apogee altitude, and based on the simulation data in this paper, it is possible to state that the

dispersion due to thrust misalignment is considerable in a comparison with that arising from other factors. Therefore, once again, we can assert the importance of studying rocket flight dispersion due to thrust misalignment in the preliminary design phase.

3.2.3 Flight Dispersion Reduction by Spinning the Rocket

In this part, we study how the spin motion of the rocket can affect the flight dispersion data. The fins at the first and second stages are canted deliberately in an effort to spin the sounding rocket through axial aerodynamic moments. Table 4 shows the normalized areas of the 95% confidence ellipses for various combinations of the first- and second-stage cant angles δ_1 and δ_2. Here, the data are normalized with the area of the ellipse corresponding to the non-spinning rocket. The mean payload-release altitude data are presented in Table 5. Figure 16 illustrates the variations of the normalized dispersion area with respect to the cant angles. From this figure, we can observe that the dispersion almost depends only on the first-stage cant angle δ_1. As shown in Fig. 15, the first-stage thrust misalignment, which occurs at a low altitude, may cause a profound effect on the trajectory of the rocket. Therefore, by canting the first-stage fins, the flight dispersion may be reduced significantly through the spin motion of the rocket right after launch. As shown in Fig. 17, the dispersion decreases with an increase of the maximum spin rate during the burn of the first-stage motor ω_1. By increasing the spin rate, the thrust misalignment averages out, and the dispersion is minimized.

Regarding the payload-release altitude, with increases of fin cant angles, this quantity tends to be lower due to the larger drag coefficient. However, it should be noted that this effect is extremely small.

As indicated above, canting the fins at the first stage is effective in reducing the dispersion area while that of the second-stage fins is proved to be inconsiderable. Moreover, a large cant angle at the second stage causes a significant spin rate during the burn of the second-stage motor. As shown
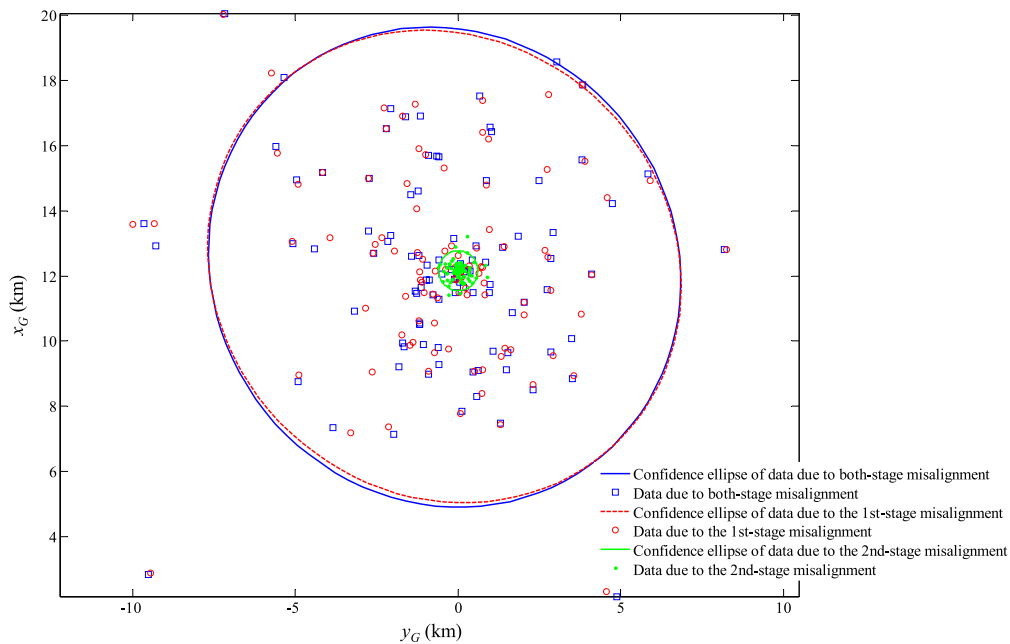
Fig. 15 The dispersion of the payload-release point for several cases of thrust misalignment

Table 4 Normalized area of the 95% confidence ellipse for various combinations of δ_1 and δ_2

$\delta_1(°)/\delta_2(°)$	0	0.1	0.2	0.3	0.4	0.5
0	1.00	0.71	0.66	0.63	0.55	0.51
0.1	0.98	0.68	0.65	0.62	0.54	0.50
0.2	0.97	0.66	0.64	0.61	0.54	0.50
0.3	0.96	0.65	0.65	0.61	0.54	0.51
0.4	0.94	0.66	0.66	0.63	0.55	0.52
0.5	0.91	0.65	0.66	0.62	0.54	0.51

Table 5 Mean payload-release altitude in km for various combinations of δ_1 and δ_2

$\delta_1(°)/\delta_2(°)$	0	0.1	0.2	0.3	0.4	0.5
0	47.43	47.27	47.25	47.25	47.29	47.27
0.1	47.48	47.28	47.27	47.26	47.28	47.25
0.2	47.51	47.28	47.26	47.25	47.28	47.24
0.3	47.49	47.23	47.24	47.24	47.25	47.21
0.4	47.45	47.22	47.22	47.23	47.23	47.18
0.5	47.43	47.18	47.19	47.20	47.21	47.14

Fig. 16 The normalized dispersion area at various values of δ_1 and δ_2

adverse effects on rocket flight while the fins at the first stage could be canted at a value as large as 0.5°. It is noteworthy that a larger value of the first-stage fin angle δ_1 may have a greater effect on the reduction of the dispersion area; however, the maximum spin rate will increase, too. To compromise between these two factors, a value of 0.5° is selected, and the corresponding maximum spin rate is around 26 rad/s according to Table 1.

Figure 18 shows the dispersion data of spinning and non-spinning rockets. For the spinning rocket, the first- and second-stage cant angles δ_1 and δ_2 are 0.5° and 0.1°, respectively. The area of the 95% confidence ellipse is about halved

in Table 2, when the second-stage cant angle is 0.5°, the maximum spin rate of the rocket is around 64 rad/s, which is regarded as extremely large and may cause severe damage to the on-board equipment. In general, the second-stage cant angle δ_2 should be held low to avoid the above mentioned
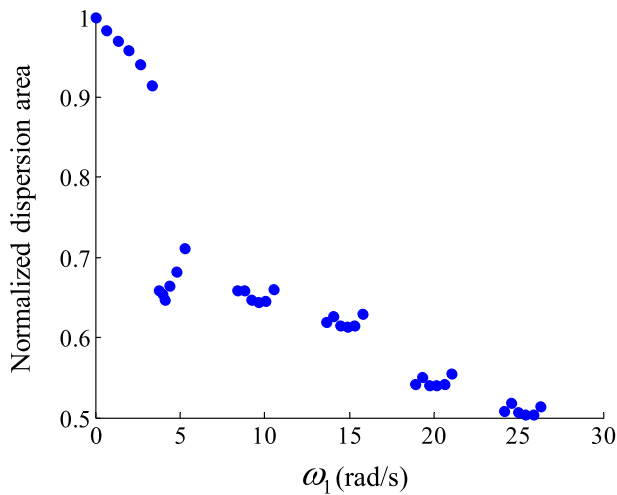
Fig. 17 The relationship between the normalized dispersion area and the maximum spin rate during the burn of the first-stage motor

from 167.8 km^2 to 84.6 km^2 when the spinning technique is applied.

For better understanding of the flight dispersion reduction, the detailed trajectory data of a specific case are analyzed. In this case, the thrust misalignment angles (angle φ in Fig. 12) of the first- and second-stage motors are given randomly and equal 0.2° and 0.3°, respectively. Similarly, angle θ takes random values of -70° and -50° respectively for the first and second stages. For the case of the spinning rocket, the fins at the both stages are assumed to be canted at 0.5°. Figure 19 shows the altitude, the downrange and the lateral deflection in the cases of the non-spinning and spinning rockets together with the ideal trajectory without thrust misalignment. It is

seen that when the rocket spins, the trajectory becomes closer to the expected one. The lateral deflection is reduced from 7.7 km to 5.1 km. In terms of speed, the spin motion does not cause any noticeable effect as shown in Fig. 20. However, there is a significant change in the orientation of the velocity vector. Figure 21 presents the deflection of the velocity vector from the longitudinal vertical plane (plane $x_G O z_G$). According to the data in this figure, the spin motion decreases the final deflection angle of the velocity vector from 27° to 21.5°. It is also shown that most of the deflection comes from the misalignment of the first-stage thrust vector, which agrees with the statistical analysis result shown in Fig. 15. The similar trend is seen in Fig. 22 for the deflection angle of the rocket body axis from the longitudinal vertical plane. The large thrust of the first-stage motor can cause significant deflections as shown in Figs. 21 and 22 when its vector and the body axis are misaligned. Moreover, due to the lower speed during this phase (Fig. 20), the rocket becomes easier to be deflected from its expected trajectory. From Fig. 22 we can see that while the rocket is spinning, its own body axis also fluctuates strongly during the burn of the motors.

Figures 23 and 24 provide the variations of the body pitch angle and the angle of attacks in different cases. We can recognize that the spinning rocket has a similar pitch angle variation to that of an ideal case without thrust misalignment. As for the angle of attack, the variation in the non-spinning case is characterized by the frequencies of the vibrations in the pitch and yaw directions while for the spinning case, in addition to these vibrations, the angle of attack also varies together with the spinning motion of the rocket about its own axis.
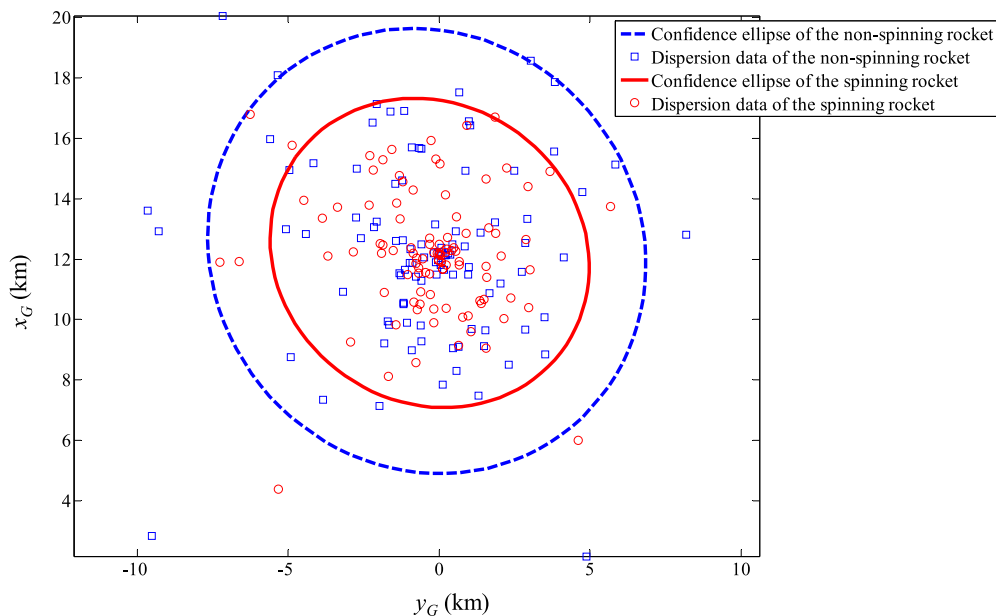
Fig. 18 The payload-release location dispersion of spinning and non-spinning rockets
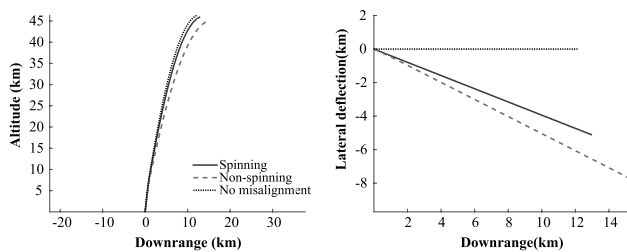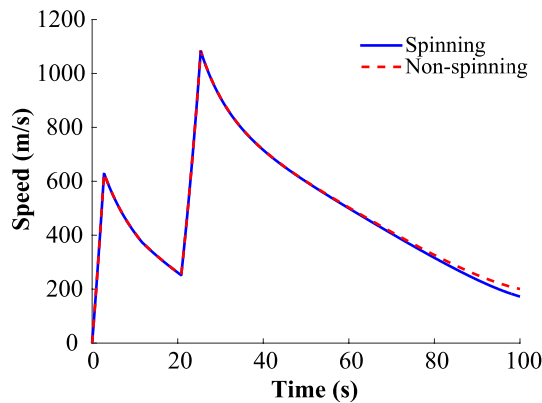
Fig. 19 The rocket trajectory in different cases

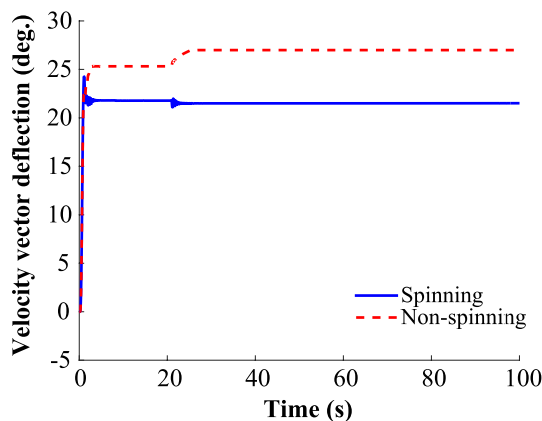
Fig. 20 The speed of the spinning and non-spinning rockets

Fig. 21 Velocity vector deflection of the spinning and non-spinning rockets
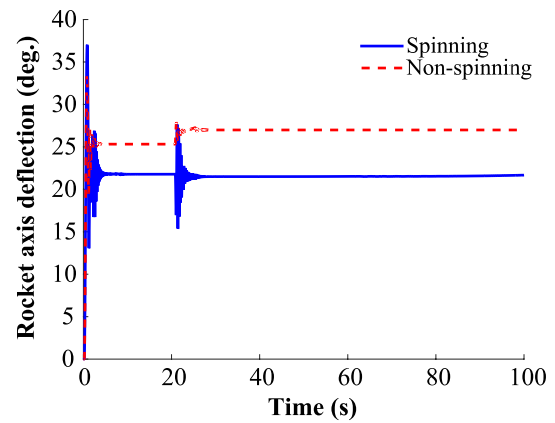

Fig. 22 The deflection angle of the rocket body axis in the spinning and non-spinning cases
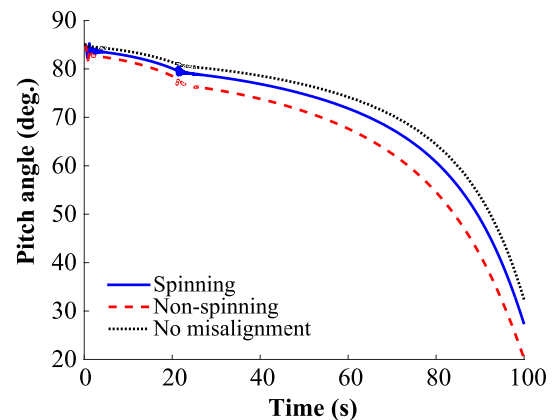
Fig. 23 The pitch angle of the rocket in different cases

3.2.4 Effect of Fin Size on the Dispersion

Here, we study the size effect of the first-stage fins, which have a great impact on the dispersion area. In addition to the model with the original fins, two others with the modified fin size are investigated (Fig. 25). The dimensions of the small and large fins are decreased and increased by 25%, respectively. The simulation process runs for the three rocket models with the cant angle of the first-stage fins of 0°, 0.1°, 0.2°, 0.3°, 0.4° and 0.5° while the second-stage fins are not canted. Figure 26a shows that the fin size has a great effect on the dispersion area. When the fins are canted at 0.5°, the maximum spin rate of the rocket before the separation of the first stage ω_1 in all cases are similar and at around 25 rad/s; however, the dispersion area of the rocket with the small fins is increased by 2.6 times from 86.1 km^2 to 226.4 km^2 whereas using the large fins reduces this area to 46.7 km^2. The big differences in the dispersion area between the cases are related to the pitch-damping coefficient. Larger fins provide larger damping in the pitch motion; therefore, the rocket becomes more stable when it is affected by thrust misalignment. It should be noted that the fin size does not have a considerable influence on the spin rate. As indicated by Eq. (21), the spin rate is a function of the ratio between the derivative coefficient of the roll moment with respect to the fin cant angle $m_{x\delta}$ and the spin-damping coefficient $mx\omega x^*$. When the size of the fins increases, these both coefficients become larger; however; their ratio is not affected
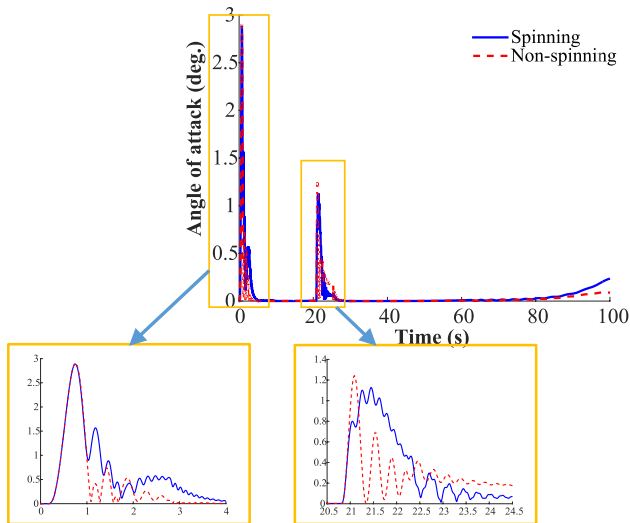
Fig. 24 The angle of attack of the spinning and non-spinning rockets
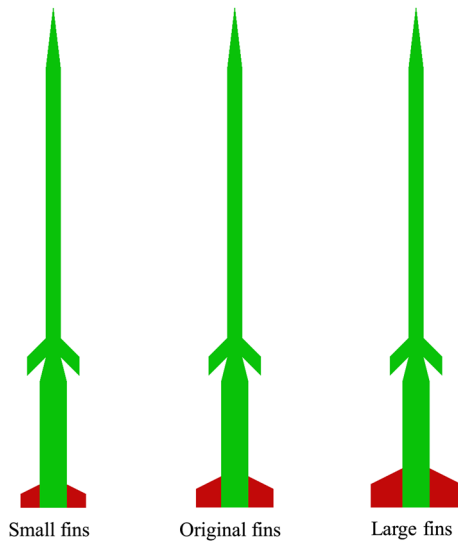

Fig. 25 Three rocket models with different fin size

significantly. Despite of the noticeable fin size effect on the dispersion area, the effectiveness of the spin motion in the reduction of this area tends to be unaffected as shown by Fig. 26b. In this figure, the area is normalized with its maximum value when the fins are not canted. It is seen that for all rocket models, the dispersion area decreases by approximately 50% when the maximum spin rate is around 25 rad/s.

In general, using larger fins seems to be more favorable in terms of stabilizing the rocket flight path due to thrust misalignment. However, a sounding rocket with large fins may be susceptible to the weathervane effect, which causes a considerable deflection of the flight path due to horizontal wind [20].
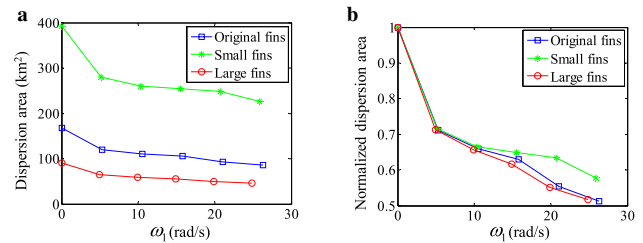

Fig. 26 Three rocket models with different fin size

4 Conclusions

This paper presents the effectiveness of spin motion in reducing the flight dispersion of a two-stage solid-propellant sounding rocket model due to thrust misalignment. The aerodynamic coefficients of the rocket are determined by the combination of semi-empirical equations and a potential-based panel method that works for both subsonic and supersonic flows. The dynamics model is developed to solve the 6-DOF equations of motion while taking the variations of the inertial parameters into consideration. Through Monte Carlo simulation techniques, it is found that thrust misalignment at the first stage has a considerable effect on the dispersion of sounding rocket flight while the effect due to the second-stage thrust misalignment is small. Moreover, the results show that by canting the fins at the first stage, the rocket starts spinning right after launch, then flight is stabilized and the dispersion can be reduced significantly. However, canting the fins at the second stage may not be necessary as it does not have any substantial effect in terms of dispersion reduction while an unfavorable extremely high spin rate may occur at a large angle. According to the analysis, if the fins at the first stage are canted at 0.5°, the area of the 95% confidence ellipse of the payload-release location is expected to be halved. The paper also exhibits an important effect of the fin size on the dispersion area. Even though the effectiveness of the spin motion tends to be independent of the fin size, using larger fins shows a positive effect on the dispersion reduction. However, the rocket with the larger fins may be more susceptible to the weathervane effect due to horizontal wind, which is not discussed in this paper.

References

1. Seibert G (2006) The history of sounding rockets and their contribution to European space research. ESA History Study Reports.
2. Christe S, Zeiger B, Pfaff R, Garcia M (2016) Introduction to the special issue on sounding rockets and instrumentation. J Astron

Instrument 05(01):1602001. https://doi.org/10.1142/S2251171716020013

3. Anderson L, Andersson J (1976) Development of the S19 guidance system for the reduction of sounding rocket dispersion. In: AIAA 4th Sounding Rocket Technology Conference. pp 172–178.

4. Knauber RN (1996) Thrust misalignments of fixed-nozzle solid rocket motors. J Spacecr Rocket 33(6):794–799. https://doi.org/10.2514/3.26840

5. Electronic Code of Federal Regulations (2020) Title 14, Part 417—Launch safety. Federal Register. https://www.ecfr.gov/cgi-bin/text-idx?SID=4539ad3af6ec0c3382cb67c775d1c66c&mc=true&tpl=/ecfrbrowse/Title14/14cfr417_main_02.tpl, Accessed 03 January 2021

6. Dunaway GL, Hoidale MM (1969) Unguided rocket impact dispersion at white sands missile range, New Mexico (September 1969). Army electronics command white sands missile range Nm atmospheric sciences office.

7. Boersma G, Bosgra J, Kruisbrink H, Schmeitink C (1970) Comparison of the impact dispersion of unguided and guided sounding rockets with further evaluation of a velocity controlled rocket. In: 2nd Sounding Rocket Technology Conference. https://doi.org/10.2514/6.1970-1381

8. Novlan DJ (1977) Unguided rocket impact dispersion at white sands missile range, New Mexico (Revision). US Army Electronics Command, ADA041587 https://apps.dtic.mil/sti/citations/ADA041587

9. Box S, Bishop CM, Hunt H (2011) Stochastic six-degree-of-freedom flight simulator for passively controlled high-power rockets. J Aerosp Eng 24(1):31–45. https://doi.org/10.1061/(ASCE)AS.1943-5525.0000051

10. Scheurpflug F, Kallenbach A, Cremaschi F (2012) Sounding rocket dispersion reduction impact by second stage pointing control. J Spacecr Rocket 49(6):1159–1162. https://doi.org/10.2514/1.A32193

11. Tsiotras P, Longuski JM (1993) Analytic solutions for a spinning rigid body subject to time-varying body-fixed torques, part II: time-varying axial torque. J Appl Mech 60(4):976–981. https://doi.org/10.1115/1.2901011

12. Javorsek DI, Longuski JM (2000) Velocity pointing errors associated with spinning thrusting spacecraft. J Spacecr Rocket 37(3):359–365. https://doi.org/10.2514/2.3586

13. Longuski JM, Gick RA, Ayoubi MA, Randall LA (2005) Analytical solutions for thrusting, spinning spacecraft subject to constant forces. J Guid Control Dyn 28(6):1301–1308. https://doi.org/10.2514/1.12272

14. Van Der Ha JC, Janssens FL (2005) Jet-damping and misalignment effects during solid-rocket- motor burn. J Guid Control Dyn 28(3):412–420. https://doi.org/10.2514/1.3852

15. Ayoubi MA, Longuski JM (2009) Asymptotic theory for thrusting, spinning-up spacecraft maneuvers. Acta Astronaut 64(7):810–831. https://doi.org/10.1016/j.actaastro.2008.12.015

16. Ayoubi MA, Martin KM, Longuski JM (2014) Analytical solution for spinning thrusting spacecraft with transverse ramp-up torques. J Guid Control Dyn 37(4):1272–1282. https://doi.org/10.2514/1.62695

17. Liang Z, Liao W, Zhang X (2019) Velocity pointing error reduction for symmetric spinning spacecraft via a two-burn scheme. Trans Inst Meas Control 41(14):3877–3886. https://doi.org/10.1177/0142331219841106

18. Jarmolow K (1957) Dynamics of a spinning rocket with varying inertia and applied moment. J Appl Phys 28:308. https://doi.org/10.1063/1.1722736

19. Bullard C, Papis T (1967) Determination of the attitude of a spinning rocket under thrust with statistically varied inputs. In: AIAA Guidance, Control, and Flight Mechanics Conference, 1967.

20. Wilde PD (2018) Range safety requirements and methods for sounding rocket launches. J Space Saf Eng 5(1):14–21. https://doi.org/10.1016/j.jsse.2018.01.002

21. Woodward FA (1968) Analysis and design of wing-body combinations at subsonic and supersonic speeds. J Aircr 5(6):528–534. https://doi.org/10.2514/3.43979

22. Lebedev AA, Chernobrovkin LS (1973) Dinamika poleta bespilotnykh letatel'nykh apparatov (Unmanned Aerial Vehicle Flight Dynamics). Mashinostroenie, Moscow ((**In Russian**))

23. Fleeman EL (2001) Tactical missile design. AIAA

24. R. C (2017) NASA-AMES WingBody Panel Code. Public domain aeronautical software. http://www.pdas.com/wingbody.html, Accessed 03 January 2021

25. Zhang WD, Wang YB, Liu Y (2013) Aerodynamic study of theater ballistic missile target. Aerosp Sci Technol 24(1):221–225. https://doi.org/10.1016/j.ast.2011.11.010

26. Ahn J, Seo J (2013) Instantaneous impact point prediction using the response-surface method. J Guid Control Dyn 36(4):958–966. https://doi.org/10.2514/1.59625

27. Jo B-U, Ahn J, Roh W-R (2020) Instantaneous impact point guidance considering uncertainty in engine cutoff time. J Guid Control Dyn 43(2):373–382. https://doi.org/10.2514/1.G004703

28. Barton MV (1950) The effect of variation of mass on the dynamic stability of jet-propelled missiles. J Aeronaut Sci 17(4):197–203. https://doi.org/10.2514/8.1592

29. Chowdhury S, Beaujardiere JPDL, Brooks M, Roberts L (2011) An integrated six degree-of-freedom trajectory simulator for hybrid sounding rockets. In: 49th AIAA Aerospace Sciences Meeting including the New Horizons Forum and Aerospace Exposition, Orlando, Florida, 2011. https://doi.org/10.2514/6.2011-1223

30. Huh J, Ahn B, Kim Y, Song H, Yoon H, Kwon S (2017) Development of a university-based simplified H2O2/PE hybrid sounding rocket at KAIST. Int J Aeronaut Space Sci 18:512–521. https://doi.org/10.5139/IJASS.2017.18.3.512

31. Peng W, Zhang Q, Yang T, Feng Z (2017) A high-precision dynamic model of a sounding rocket and rapid wind compensation method research. Adv Mech Eng 9(7):1–11. https://doi.org/10.1177/1687814017713944

32. Thomson WT (1966) Equations of motion for the variable mass system. AIAA J 4(4):766–768. https://doi.org/10.2514/3.3544

33. Eke FO (1998) Dynamics of variable mass systems. NASA Tech Rep

34. Nguyen AT, Han J-H, Vu TT (2019) The effects of wing mass asymmetry on low-speed flight characteristics of an insect model. Int J Aeronaut Space Sci 20(4):940–952. https://doi.org/10.1007/s42405-019-00165-6

35. McDaniel M, Evans C, Lesieutre D (2010) The effect of tail fin parameters on the induced roll of a canard-controlled missile. In: 28th AIAA Applied Aerodynamics Conference, 2010. https://doi.org/10.2514/6.2010-4226

36. Wang B, Shi W, Miao Z (2015) Confidence analysis of standard deviational ellipse and its extension into higher dimensional euclidean space. PLoS ONE 10(3):e0118537–e0118537. https://doi.org/10.1371/journal.pone.0118537

37. Electronic Code of Federal Regulations (2020) Title 14, Part 420—License to operate a launch site. Federal Register. https://www.ecfr.gov/cgi-bin/text-idx?SID=4539ad3af6ec0c3382cb67c775d1c66c&mc=true&tpl=/ecfrbrowse/Title14/14cfr420_main_02.tpl, Accessed 03 January 2021